Perovskite oxygen carrier with chemical memory under reversible chemical looping conditions with and without SO_2 during reduction

Lei Liu[a], Zhenshan Li*[a], Zuoan Li[b], Yngve Larring[b], Ningsheng Cai[a]

a. Key Laboratory for Thermal Science and Power Engineering of Ministry of Education, Department of Energy and Power Engineering, Tsinghua University, Beijing 100084, China

b. SINTEF Industry, Sustainable Energy Technology, P.O. Box 124 Blindern, NO-0314 Oslo, Norway

*Corresponding Author

Telephone number: +86-10-62789955

E-mail address: lizs@mail.tsinghua.edu.cn

Abstract

Oxygen carrier materials (OCM) are usually exposed to sulfur-contained gases in the fuel reactor for chemical looping combustion. This work provides both experimental and model work to understand the SO_2 effect on the heterogeneous redox kinetics of a $CaMn_{0.375}Ti_{0.5}Fe_{0.125}O_{3-\delta}$-based perovskite oxygen carrier. The cycle reactivity and redox kinetics under reducing conditions were conducted with and without SO_2 in a micro-fluidized bed thermogravimetric analysis technology (MFB-TGA). The redox kinetic behaviors were simulated by a bubbling fluidized bed reactor model coupled with a two-stage kinetic model. The SO_2 can react with the perovskite to increase the oxygen transfer capacity from 4 wt% to 5 wt%. When the temperature is higher than 1173 K, SO_2 has almost no effect on the H_2 reduction reactivity, while the oxidation reactivity decreases by 50 %, but the oxidation is still fast enough to achieve 4 wt% capacity within 8 s. When the temperature is lower than 1173 K, there is a significant sulfur-poisoning effect during oxidation and reduction. The

analyses of XRD, SEM-EDS, and in-situ DRIFTS indicated that most of the absorbed sulfur mainly existed in the sulfate/sulfide shell on the particle surface. The chemical kinetics and physical structure of $CaMn_{0.375}Ti_{0.5}Fe_{0.125}O_{3-\delta}$ perovskite can be completely recovered in the absence of SO_2, and this perovskite oxygen carrier is chemically memorable and reversible in its solid structure. The fundamental understanding of the sulfur effect on the redox kinetics and solid structure of the perovskite oxygen carrier provides a new insight to the material development and corresponding reaction mechanisms.

Keywords: Chemical looping combustion; Oxygen carrier material; $CaMnO_3$, Perovskite oxide; sulfur; Kinetics

1. Introduction

Chemical looping combustion (CLC) has emerged as a promising technology to capture CO_2 from fossil fuel combustion for power and heat generation [1,2]. A typical CLC unit usually consists of an air reactor and a fuel reactor. A solid oxygen carrier material (OCM) circulates between the reactors, to deliver the required lattice oxygen for fuel conversion in the fuel reactor. Then, the reduced OCM experiences an oxidization step in the air reactor. Developing an OCM with fast reactivity, high stability, as well as high attrition resistance, is the key to the CLC technology [3]. Up to now, both natural minerals and manufactured OCMs have been applied in the CLC process [3,4]. Generally, these OCMs are metal oxides from manganese (Mn) [5,6], iron (Fe) [7], copper (Cu) [8], nickel (Ni) [9], etc. To further improve the physical and chemical properties of OCMs, some bimetallic OCMs have been developed, such as Cu-Fe-based [10], Ni-Mn-based [11], and Cu-Mn-based [12] OCMs, etc. For transition metal oxide OCMs, phase change during redox cycles has often been observed, resulting in materials degradation, agglomeration, i.e. shorter life time.

Recently, synthetic OCMs with perovskite-type structures ($ABO_{3-\delta}$) have attracted increasing interest for CLC applications thanks to the fast oxygen bulk diffusion and surface exchange during the consecutive redox cycles, as well as their redox and stability which can be tuned by varying doping elements and their concentrations on both A and B sites [13-15]. Enormous efforts have been devoted to improving OCMs' reactivity and recyclability performance of OCMs based on $CaMnO_{3-\delta}$. For example, researchers substituted Ti, Fe or Mg into $CaMnO_{3-\delta}$ structure to selectively change the cationic site, to improve reactivity, stability, crushing strength, fluidization property, etc. [14, 16-21]. The investigations mainly focused on the determination of chemical redox reactivity and heterogeneous gas-solid reaction kinetics at variable temperatures and gas atmospheres (O_2, H_2, CO, CH_4), and partial pressures under sulfur (S)-absence condition [17-19]. The $CaMn_xB_{1-x}O_{3-\delta}$ (B= Fe, Ti, Mg etc.) OCMs have shown promising chemical properties for the CLC process as long as sulfur (S) is absent [17-19, 22]. However, sulfur (S) is widely present in fossil fuels, which means the OCM has to expose to sulfur-containing species in the fuel reactor. The previous studies found that the chemical reactivity of the $CaMn_xB_{1-x}O_{3-\delta}$suffered from deactivation due to calcium sulfate formation, once exposed to the situation of sulfurous fuels [23-25]. In these researches, CH_4 with different sulfur contents was used as the fuel to assess the chemical performance of OCMs [23-25]. However, the major reducing gas compositions for solid fuels are CO and H_2 from the devolatilization and gasification steps in the fuel reactor of CLC, and CH_4 content is normally very low in the fuel reactor. Therefore, the conclusions or results regarding sulfur effect on chemical performance by utilizing CH_4 fuel, cannot be used directly when evaluating solid fuel CLC, e.g. reactor design. Up to now, the determination of heterogeneous reaction kinetics and insight to the influence mechanism of the fuel in the presence of SO_2 are very limited due to insufficient

experiments and characterizations. In the previous work, $CaMn_{0.375}Ti_{0.5}Fe_{0.125}O_{3-\delta}$ particles as OCMs were controllably fabricated via spray drying granulation, and the heterogeneous reaction kinetics was investigated without SO_2 containing gases [26]. Heterogeneous redox reaction kinetics in the presence of SO_2 is more closely associated with the chemical performance evaluation, reactor design and optimization for the solid fuel CLC. However, the influence of SO_2 on the reactivity and redox kinetic behaviors is still partially unknown.

In this work, the investigation of oxidization and reduction kinetics with and without SO_2 was conducted by means of a micro-fluidized bed thermogravimetric analysis technology (MFB-TGA), based on real-time mass change measurement of OCM particles in a fluidizing state close to enhanced mass and heat transfer in a real CLC reactor [27,28]. The redox kinetic behaviors were described by a simplified K-L model coupled with a two-stage kinetic model via changing the chemical reaction rate constant (k_{chem}, k_{diff}), and the ratio of the conversion level at the fast reaction stage to the conversion level (Ψ). The OCM was characterized by X-ray Fluorescence (XRF), scanning electron microscope (SEM), energy dispersive spectrometer (EDS) mappings, X-ray diffraction (XRD), and in-situ reflectance infrared spectroscopy (DRIFTS).

2. Experimental

2.1. Oxygen carrier material

The perovskite oxide, $CaMn_{0.375}Ti_{0.5}Fe_{0.125}O_{3-\delta}$, was fabricated as the OCM particles employing spray granulation followed by a calcination stage at 1623 K for 12 h [26]. Particle size in the range of 180-250 μm was used to investigate the reaction kinetics. X-ray Fluorescence (XRF) results show that the compounds of the oxidized OCM are 40.52 wt% CaO, 26.38 wt% TiO_2, 22.94 wt% MnO and 7.07 wt% Fe_2O_3. More properties of the OCM are listed in Table 1. The true density

(ρ_t) was measured by a helium replacement method (AccuPyc II 1345, Micromeritics). The porosity was analyzed by a mercury intrusion porosimetry (AutoPore IV 9500, Micromeritics). The surface area was obtained by Brunauer–Emmett–Teller (BET) using a nitrogen adsorption instrument at 77 K (ASAP 2460, Micromeritics).

Table 1 Physical properties of the oxidized and reduced $CaMn_{0.375}Ti_{0.5}Fe_{0.125}O_{3-\delta}$

State	d_p(μm)	ρ_t(kg/m^3)	Porosity	BET(m^2/g)
Oxidized	180-250	4910	0.493	0.26
Reduced		4898	0.489	0.35

2.2. Micro-fluidized bed thermogravimetric analysis (MFB-TGA)

The chemically oxidizing and reducing kinetics of the perovskite particles was determined via a micro-fluidized bed thermogravimetric analysis technology (MFB-TGA) [27,28]. The main components include a heating furnace, a fluidized-bed reactor, a gas supply unit, and a measurement unit, among which, the core is the fluidized-bed reactor with an inner diameter of 30 mm (Fig. 1). The flowrates of the fluidizing agents were controlled at 1.2-1.5 L/min (STP), which ensures that the fluidized-bed reactor was operated at a bubbling state during the measurements. The switch among different fluidizing agents into the bottom of the bubbling-bed reactor uses well-connected magnetic valves. A mass transducer with a readability of 1 mg was employed to measure the on-line mass change caused by chemical gas-solid reactions. A K-type thermocouple enclosed in the bubbling-bed reactor was employed to measure bed temperature. A differential pressure transducer was employed to monitor the pressure drop of the bubbling-bed reactor. More details can be found elsewhere [26-28].

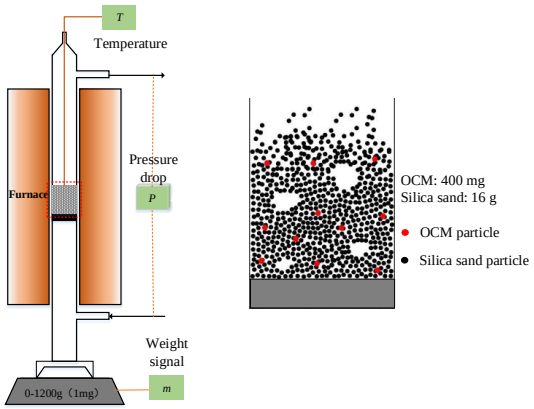

Fig. 1. Schematic diagrams of the MFB-TGA apparatus

For a typical experiment of redox kinetics, ~ 16 g silica sand with the particle size at 300-355 μm was firstly filled as the inert bed material, followed by ~ 400 mg fully oxidized OCM particles injected into the bubbling-bed reactor after heating up to the desired temperature under a 21 vol% O_2 fluidizing agent (Fig. 1). After the stable mass and temperature signals were reached, fluidizing gases switch between the reducing gases (10 % H_2 with 500 ppm SO_2 or 10 % H_2 without SO_2) and oxidizing gas (21 vol% O_2) was conducted for redox cycles. Inert gas was flowed into the reactor for 30 s between the oxidizing and reducing steps, to prevent direct mixing of H_2 and O_2. 500 ppm SO_2 was mixed with the reducing gas to create a sulfur exposure atmosphere and simulate a more real condition in the CLC process of the sulfur-containing fuels. Operating at the superficial velocity of 3-5 U_{mf}, the oxidization and reduction rates were obtained at 1023-1173 K. Redox cycles were repeated at least 3 times to ensure reproducibility at each temperature. Table 2 concludes the experimental scheme of the kinetic determination under condition with or without SO_2. Series I-IV were used to investigate the evolution of reaction kinetics under reduction condition with SO_2. Series V was performed to regenerate the sulfur-poisoned OCM under the reduction condition without SO_2. Finally, the redox kinetics of the poisoned and recovered OCM at 1023-1173 K was determined. Another multicyclic test, similar to Series I-IV, was performed under reducing condition

without SO_2 for comparison.

Table 2. Experimental scheme of determining the reaction kinetics under sulfur-presence/absence condition

Series	Temperature	Fluidizing agents	Periods	No of cycles
I	1173 K	$O_2/H_2(SO_2)$	120s/480s	2
II	1173 K	$O_2/H_2(SO_2)$	120s/180s	3
III	1173K	$O_2/H_2(SO_2)$	60s/180s	2
IV	1173K	$O_2/H_2(SO_2)$	60s/120s	43
V	1173K	O_2/H_2(no SO_2)	60s/120s	15

The balance gases in the reaction agents (10 vol% H_2 with 500 ppm SO_2 or 10 vol% H_2 without SO_2 and 21 vol% O_2) were well matched to ensure similar densities as inert gas (33.22 vol% He in 66.78 vol% Ar), see Table 3. In this regard, the noise possibly created by gases switch was eliminated. Finally, the impact of the gas switches on the on-line mass signals was eliminated, and the measurement error of the MFB-TGA is kept within ±1 mg, see Fig. 2. Therefore, the on-line mass change was only caused by the heterogeneous gas-solid reactions, as shown from a typical redox cycle in Fig. 3.

Table 3. The compositions of the reaction gases and the balance gases

Reaction gas	Inert gas
10 vol% H_2+21.65 vol% He + 68.35 vol% Ar	33.22 vol% He+66.78 vol% Ar
10 vol% H_2+500 ppm SO_2+21.65 vol% He + 68.35 vol% Ar	33.22 vol% He+66.78 vol% Ar
21 vol% O_2+28.59 vol% He + 50.41 vol% Ar	33.22 vol% He+66.78 vol% Ar

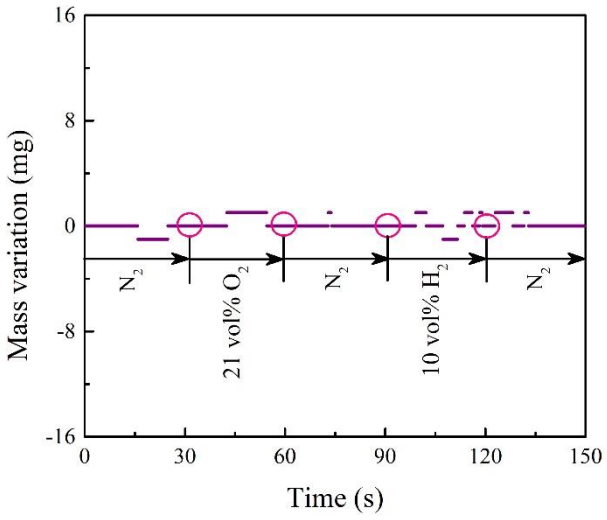

Fig. 2. Blank test of the gas switch at 1173 K (only 16.4 g silica sand was filled as the bed materials without OCM particle). The mass fluctuation is ±1 mg for the blank test.

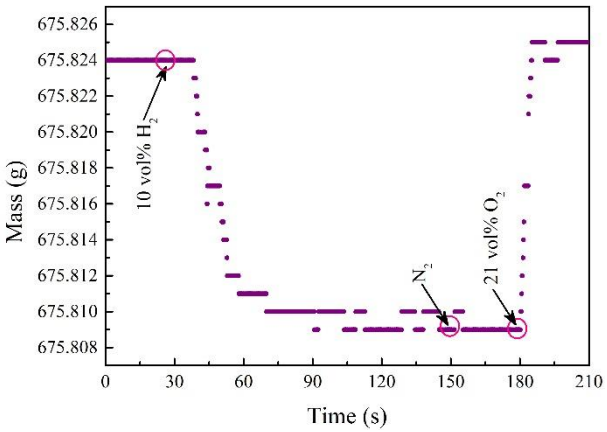

Fig. 3. A typical redox test at 1173 K: the bed materials consists of 16 g silica sand and 400 mg OCM particles, and the experimental data were obtained by switching the reaction agents between 10 vol% H_2 and 21 vol% O_2.

2.3. Post characterizations

To determine possible sulfur effects on the surface OCM particles, in-situ diffuse reflectance infrared Fourier transform spectroscopy (NEXUS, 870 FT-IR) was used. The mixture of 80 wt% KBr and 20 wt% OCM powders were added into a photo-reactor. A background IR spectrum was

collected in pure Ar (500 mL/min) atmosphere after pretreated at 993 K. After Ar purging for an additional 30 min, the reduction by SO_2-containing H_2 (10 vol% H_2 with 500 ppm SO_2) was conducted at 993 K for 480 s. After reduction, pure Ar was used to flush the reactor for 120 s. Then, 21 vol% O_2 was introduced for 300 s in the oxidization step, followed by another Ar purging step for 120 s. Subsequently, the above reduction and oxidization steps were repeated for 48 cycles. The IR spectra were obtained in real-time during the test.

The phase purities were obtained by X-ray diffraction (XRD) patterns (D8 Advance, BRUKER). Scans were selected between 10° and 90° with a step of 10°/min to analyze the phase compositions. The morphology characteristics of the surface and cross-section of the tested $CaMn_{0.5}Ti_{0.375}Fe_{0.125}O_{3-\delta}$ particles were characterized by a scanning electron microscope (SEM, Zeiss Merlin), and the element distributions were analyzed by an energy dispersive spectrometer (EDS).

2.4. Data evaluation

The on-line mass signals, $m(t)$, were recorded by the mass transducer during the test. The oxygen transfer capacity ($R_{oc,t}$), defined as Eq. (1), was experimentally estimated as explained below. The conversion levels for the reduction (X_r) and oxidization (X_o) reactions were calculated as Eqs. (2) and (3), respectively. m_{oc} is the mass of the added OCM particles in the fully oxidized state, while m_o and m_r are the total mass of the reactor and bed materials, corresponding the OCM particles in fully oxidized and reduced states, respectively.

$$R_{o,t}=\frac{m_o-m_r}{m_{oc}} \quad (1)$$

$$X_r(t)=\frac{m_o-m(t)}{R_{o,t}m_{oc}} \quad (2)$$

$$X_o(t)=\frac{m(t)-m_r}{R_{o,t}m_{oc}} \quad (3)$$

3. Models

In the bubble bed reactor, the OCM particles were averagely distributed in the emulsion phase together with the silica sand, whereas the reaction gases mainly existed in the bubble phase. Taking the reduction processes as an example (Fig. 4), the reaction gases in the fluidizing agents are firstly diffused from the bubble phase to the emulsion phase. After the interphase gas exchange, the reaction gases are further transferred to the OCM particle surface distributed in the emulsion phase. Finally, the gas-solid reaction occurs on the OCM particles. Therefore, there is a requirement to apply a reactor model to analyze the interphase gas diffusion in the reactor.

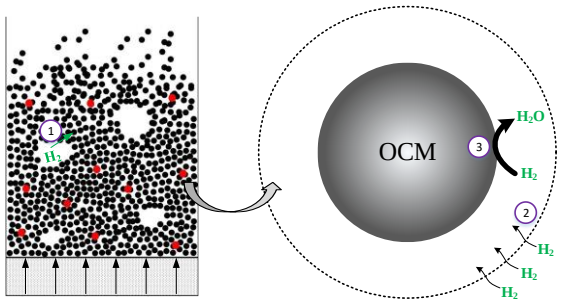

① Interphase gas interchange; ② External gas diffusion; ③ gas-solid reaction

Fig. 4. Schematic diagrams of the reduction reaction with H_2 in the bubbling bed reactor

To describe the mass transfer and chemical reaction processes in the bubbling bed reactor, a simplified reactor model was applied here, and expressed by Eqs. (4) and (5) for the bubble phase and emulsion phase according to mass balance [28]. The reactor model was based on the classic fluidization bed reactor model put forward by Kunii and Levenspiel (K-L model) [29].

$$-U_b^* \frac{\mathrm{d}C_{\mathrm{b},i}}{\mathrm{d}z} = K_{\mathrm{be}}(C_{\mathrm{b},i} - C_{\mathrm{e},i}), (i = \mathrm{O_2}, \mathrm{H_2}) \quad (4)$$

$$-(1-\theta)U_{\mathrm{mf}} \frac{\mathrm{d}C_{\mathrm{e},i}}{\mathrm{d}z} = -\theta K_{\mathrm{be}}(C_{\mathrm{b},i} - C_{\mathrm{e},i}) + f_{\mathrm{a}}(1-\theta)(1-\varepsilon_{\mathrm{mf}})K_{\mathrm{r}}C_{\mathrm{e},i}, (i = \mathrm{O_2}, \mathrm{H_2}) \quad (5)$$

where $C_{\mathrm{b},i}$ (mol/m^3) and $C_{\mathrm{e},i}$ (mol/m^3) is the gas concentration in the bubble phase and emulsion phase, respectively. U_b^* (m/s) and U_{mf} (m/s) refer to the effective gas velocity in the bubble phase and the minimum fluidization velocity. K_{be} (s^{-1}) is the gas interchange coefficient between

the bubble phase and the emulsion phase. f_a is the volume fraction of the OCM particles in all solid volume. θ is the fraction of the bubble phase, and ε_{mf} is the voidage of fluidized bed at minimum fluidization state. The supporting document introduces how to calculate the above coefficients and the analytical solution of Eqs. (4) and (5) in detail. K_r (s^{-1}) is the comprehensive reaction rate constant, including the gas-solid reactions and the impact of the external mass transfer resistance, expressed as [18,26]:

$$K_r = \frac{1}{\frac{1}{K_{ri}} + \frac{d_p}{6k_g}} \tag{6}$$

$$K_{ri} = \frac{R_{o,t}\rho_s}{\alpha M_O}\left\{k_{chem}(\psi X_e - X_{chem})^{2/3} + k_{diff}[(1-\psi)X_e - X_{diff}]^{2/3}\right\} \tag{7}$$

$$k_g = \left(Sh \cdot D_i\right)/d_p, \quad (i = O_2, H_2) \tag{8}$$

where k_g (m/s) is the external mass transfer coefficient, D_i (m^2/s) is the molecular diffusivity of gas *i*, d_p (m) is the particle size of the used oxygen carrier, Sh is Sherwood number. K_{ri} (s^{-1}) is the reaction rate constant, describing the gas-solid reactions only, and the value of K_{ri} (s^{-1}) is dependent on the conversion level of the oxygen carrier particles. A kinetic model was coupled with the reactor model here. It is well known that a gas-solid reaction commonly includes two stages, i.e., an initially fast stage and a second slow stage [30]. Some kinetic models have been developed for this purpose from literature, such as the apparent model [31], the shrinking core model [32], the pore model [33], and the grain model [34]. However, the above models fail to predict the kinetic transition behavior from the initially fast reaction stage to the second slow reaction stage [30]. In this work, a semi-empirical model containing the two reaction stages was applied to describe the conversion of the oxidation and reduction reactions, as seen in Eqs. (9)-(11) [18,26].

$$\frac{\mathrm{d}X_{\mathrm{chem}}}{\mathrm{d}t} = k_{\mathrm{chem}}(\psi X_{\mathrm{e}} - X_{\mathrm{chem}})^{2/3} C_{\mathrm{e},i}, \quad (i = \mathrm{O}_2, \mathrm{H}_2) \tag{9}$$

$$\frac{\mathrm{d}X_{\mathrm{diff}}}{\mathrm{d}t} = k_{\mathrm{diff}}[(1-\psi)X_{\mathrm{e}} - X_{\mathrm{diff}}]^{2/3} C_{\mathrm{e},i}, \quad (i = \mathrm{O}_2, \mathrm{H}_2) \tag{10}$$

$$X = X_{\mathrm{chem}} + X_{\mathrm{diff}} \tag{11}$$

where X_{chem} and X_{diff} are the conversion levels of the first stage and the second stage, X_{e} is the equilibrium conversion level. The second stage starts at the end of the fast reaction stage (critical conversion, ψX_{e}). k_{chem} ($\mathrm{m^3/mol/s}$) and k_{diff} ($\mathrm{m^3/mol/s}$) represent the reaction rate constants of the fast reaction stage and the slow reaction stage, respectively. ψ refers to the kinetic transition point. The exponent of the two stages, 2/3, is a known parameter in the model. Finally, the total conversion level of a reaction is the sum of the two stages. Based on the kinetic model, a conversion versus time curve can be obtained by giving the values of the rate constant (k_{chem} ($\mathrm{m^3/mol/s}$) and k_{diff} ($\mathrm{m^3/mol/s}$)) and ratio (ψ). Then the value of K_{ri} ($\mathrm{s^{-1}}$) can be calculated by using Eq. (4). As a result, the kinetic model is coupled with the reactor model through K_{r} ($\mathrm{s^{-1}}$).

In the model, the oxidization by O_2 and reduction by H_2 are assumed to be first-order [17,19,22]. It should be noted that the reactor model implemented with the two-stage kinetic model has an analytical solution, and the detailed calculation algorithm can be found elsewhere [18,26]. In the model, k_{chem} ($\mathrm{m^3/mol/s}$), k_{diff} ($\mathrm{m^3/mol/s}$) and ψ depend on the reaction temperature, which can be expressed as Arrhenius equations,

$$k_{\mathrm{chem}} = A_{\mathrm{chem}} \exp\left(-\frac{E_{\mathrm{chem}}}{R_g T}\right) \tag{12}$$

$$k_{\mathrm{diff}} = A_{\mathrm{diff}} \exp\left(-\frac{E_{\mathrm{diff}}}{R_g T}\right) \tag{13}$$

$$\psi = A_{\psi} \exp\left(-\frac{E_{\psi}}{R_g T}\right) \tag{14}$$

The axial distribution of the gas concentration is variable in the emulsion phase. In this work,

the average gas concentration across the whole bed in the emulsion phase calculated by Eq. (15) was applied to calculate the conversion levels in Eqs. (9) and (10).

$$C_{e,i,ave} = z^{-1}\int_0^z C_{e,i}dz,\ (i = O_2, H_2) \quad (15)$$

4. Results and discussion

4.1. Redox multicycles

The redox multicycles of the OCM at 1173 K are shown in Fig. 5. In Fig. 5(a), the whole redox process was done under the reduction condition without SO_2. The mass variation profiles are quite stable during the multicycles, implying there is no chemical degradation under the reduction condition without SO_2. The total oxygen transfer capacity is kept at approximately 4 wt% during the redox multicycles. In Fig. 5(b), the 1-50 redox cycles were conducted under the reducing condition with SO_2. It is clear that the mass variation profiles tend to rise. The mass variation profiles indicate the total oxygen transfer capacity of the OCM is progressively increasing with the redox cycle number under the reduction condition with SO_2 until 24 redox cycles, see Fig. 5(b). After that, the mass variation profiles are stable for the following 20 redox cycles, implying a chemical stability state under the reduction condition with SO_2. Afterwards, the reducing gas was altered to 10 vol% H_2 without SO_2. On the contrary, the mass variation profiles stay progressively decreasing from cycle 51 to cycle 62, following a new chemical stability state under the reduction condition without SO_2. From the fluctuation of the pressure drop profiles (Figs. 5(a) and (b)) and the high-temperature fluidization (Video 1), there is no observed sintering and agglomeration during the redox tests. It can be concluded that the OCM particles possess perfect fluidization properties.

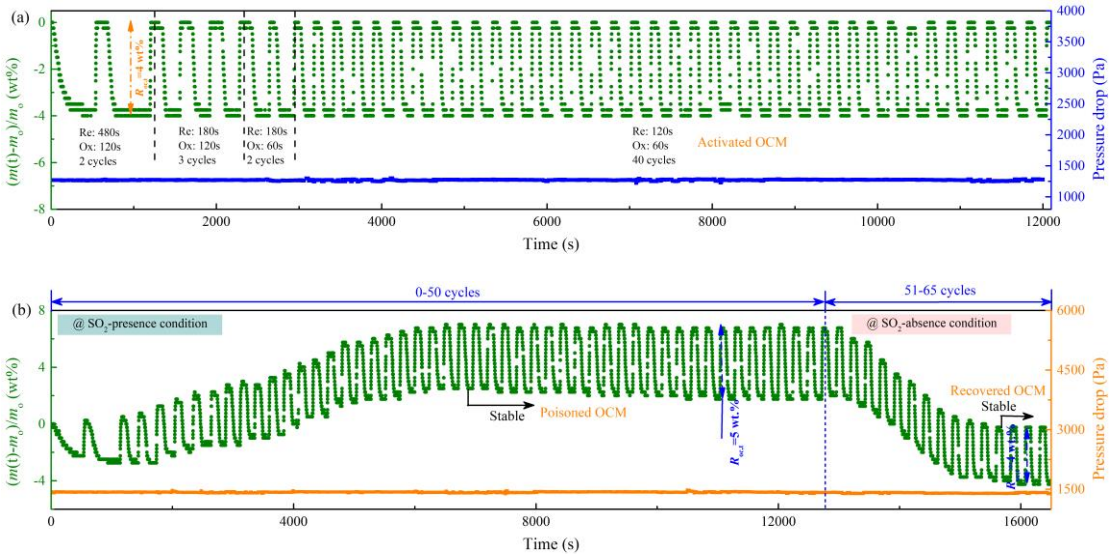

Fig. 5. Multicycles of mass variation and pressure drop during redox cycles at 1173 K (oxidization: 21 vol% O_2; reduction: 10 vol% H_2). (a) without SO_2; (b) with SO_2, reduction (1-50 cycles) : 10 vol% H_2 with 500 ppm SO_2; reduction (51-65 cycles) : 10 vol% H_2 without SO_2.

Fig. 6 compares the mass variation and oxygen transfer capacity during the redox multicycles. In Fig. 6(a), $m_{oc,r}$ refers to the mass change after reduction of each cycle, and the change of $m_{oc,r}$ with the cycle number stands for the "baseline" change during the redox multicycles. At $m_{oc,r}$, the OCM is under the reduced state. From the profiles in Fig. 6(a), the value of $m_{oc,r}$ experiences an increase from -2.25 wt% to 2 wt% with the redox cycle number when reduced with SO_2-containing H_2. After that, the value of $m_{oc,r}$ is kept unchanged from cycle 24 to cycle 50. Once switching the reduction condition to SO_2-free H_2, the value of $m_{oc,r}$ is decreasing to -4.25 wt% as the redox proceeds. Compared with the redox process without SO_2, the value of $m_{oc,r}$ stays at -4 wt% from the beginning to the end. The presence of SO_2 in the reduction step also affects the oxygen transfer capacity ($R_{oc,t}$) of the OCM, as seen in Fig. 6(b). If the OCM is reduced without SO_2, the value of $R_{oc,t}$ is always equal to 4 wt% during the whole redox multicycles. However, reduction in the presence of SO_2 would change the oxygen transfer capacity. In the whole redox process, the total

oxygen transfer capacity increases continuously from 2.3 wt% to 5 wt% under the reduction condition with SO_2, then decreases to 4 wt% after removing SO_2.

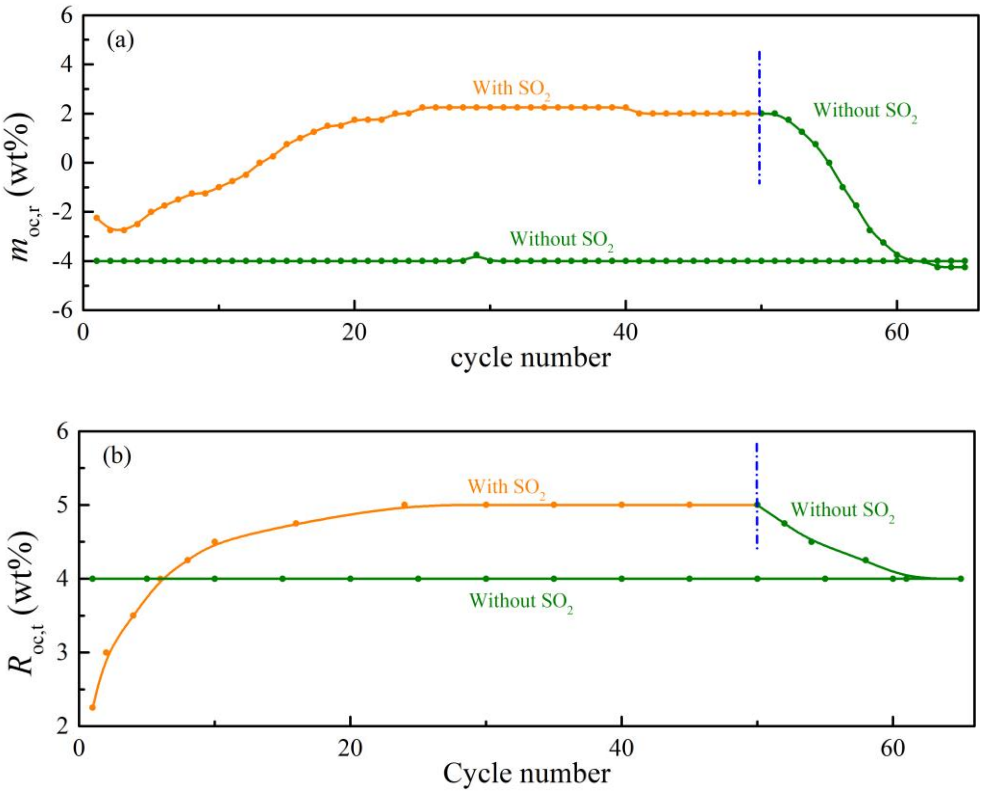

Fig. 6. Comparison of (a) mass variation and (b) oxygen transfer capacity with the cycle number

In the increasing stage of the mass variation profiles in Fig. 5(b), the reaction rates of reduction are enhanced from cycle 1 to cycle 24 (Fig. 7(a)). There is no noticeable change in reduction rates between cycle 24 and cycle 50. The depth of reduction increases from 2.25 wt% to 5 wt%, indicating that more lattice oxygen can be utilized during the reduction step. When reduced without SO_2, the reduction rates of the OCM are slightly improved with the redox cycle number, but the depth of reduction finally stabilizes to 4 wt%, see Fig. 7(b).

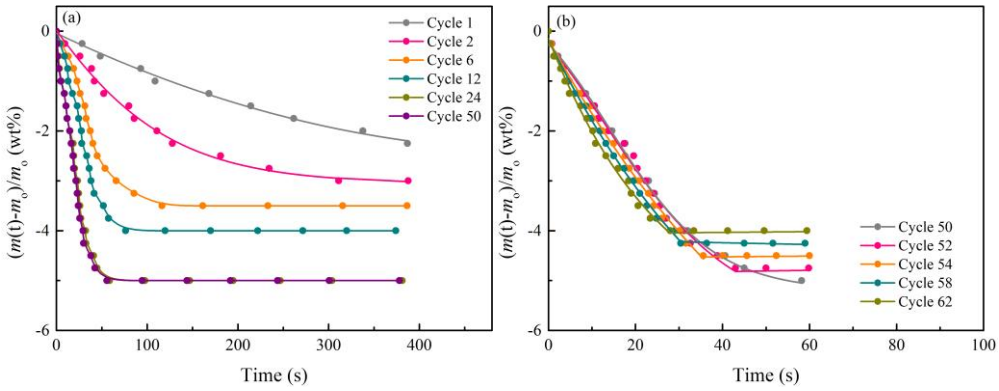

Fig. 7. Mass variation with the cycle number for the reduction process in Fig. 5(b). (a) with SO_2 and (b) without SO_2

During the first 24 cycles in Fig. 5(b), the regeneration of oxidization can take up more oxygen (O) elements in the OCM, see Fig. 8(a). For example, the mass loss is 4 wt% for the reduction of cycle 12, but 4.25 wt% oxygen (O) elements are taken up during the oxidization step. The gained oxygen (O) element by CaS oxidation to $CaSO_4$ can play an active role for the following reduction step. Hence, the oxygen transfer capacity is rising for the former 24 redox cycles. On the contrary, from cycle 50- 60 in Fig. 5(b), fewer oxygen (O) elements are taken up during the regeneration of oxidization steps due to removal of active CaS-$CaSO_4$ shell type OCM. The oxygen transfer capacity finally decreases to 4 wt%.

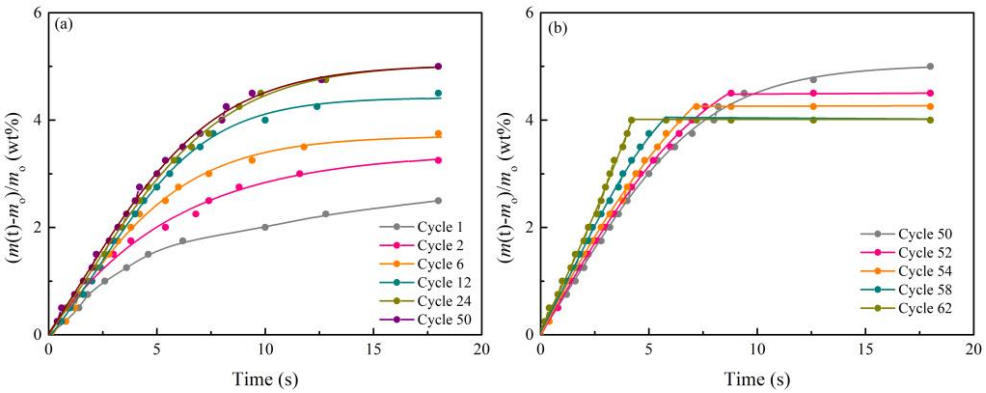

Fig.8. Mass variation with the cycle number for the oxidization process in Fig. 5(b). (a) with SO_2 and (b) without SO_2

During the multiple redox cycles under the reduction condition without SO_2, the change of chemical performance with the cycle number is demonstrated in Figs. 9(a) and (b). The reduction rate is continuously improved as the cycle number increases (Fig. 9(a)), but the oxidization rate can stabilize since cycle 6 (Fig. 9(b)). Hence the OCM shows an activation process during the redox multicycles. The reduction depth always stays at 4 wt%, hence the total oxygen transfer capacity stays unchanged during the whole process.

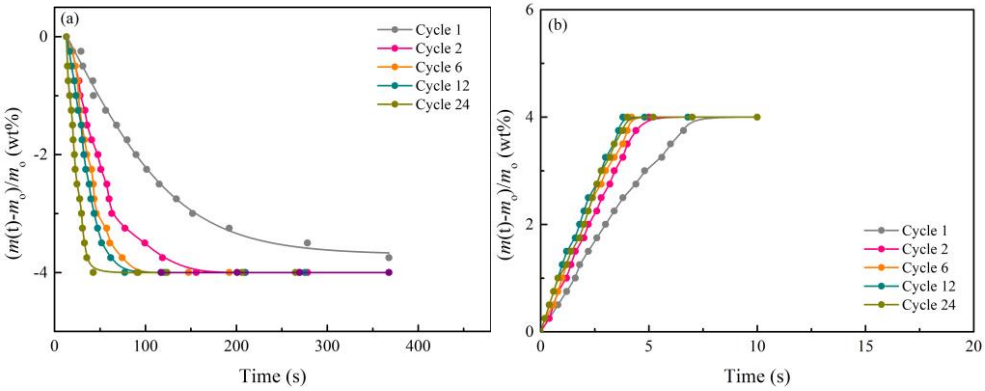

Fig. 9. Mass variation with the cycle number for the (a) reduction process and (b) oxidization process under reduction condition without SO_2 in Fig. 5(a)

It should be noted here that the perovskite oxide after 24 redox cycles is termed as "Activated OCM", as illustrated in Fig. 5(a). The "Activated OCM" is not treated by SO_2. The OCM in the chemical stability state under the reduction condition with SO_2 is called "Poisoned OCM", whereas the "Recovered OCM" means the chemically stable OCM particles under the reduction condition without SO_2, as depicted in Fig. 5(b). It can be seen that the total oxygen transfer capacity of the "Activated OCM" is equal to that of the "Recovered OCM".

4.2. Comparison of the oxidization and reduction reaction rates

Figs. 10(a) -(d) compare the reduction and oxidization reaction rates for the SO_2-poisoned and activated OCMs at 1073 K and 1173 K. When reacting at 1173 K, the reduction rate of the poisoned

OCM is very close to that of the activated OCM, and the required time for reduction to 4 wt% is ~28 s for the activated OCM and ~35 s for the poisoned OCM, respectively. However, the poisoned OCM can be further reduced due to a higher total oxygen transfer capacity. When the temperature decreases to 1073 K, the reduction rate of the activated OCM just decays a little, and the required time for full reduction is prolonged to ~60 s. Whereas the poisoned OCM is deeply affected by temperature, and the reduction rate of the poisoned OCM decreases by ~7 times, as compared to that at 1173 K. One common point for both the poisoned OCM and the activated OCM is that the reduction curves are composed of an initially fast reaction stage and a second slow reaction stage. For the oxidization reaction, the reaction rate of the poisoned OCM is slower than that of the activated OCM at 1073 K and 1173 K. For the activated OCM, the temperature has a weak impact on the oxidization rate, and the oxidization is only dominated by the initial fast reaction stage. However, for the poisoned OCM, the oxidization rate decreases a lot with decreasing temperature, and the oxidization curves consist of a fast reaction stage and a slow reaction stage, similar to the reduction curves. Although the oxidation kinetics decreased by 50% as compared to that of the activated OCM 1173 K, the oxidation of the SO_2-poisoned OCM is still fast enough and can achieve 4 wt% of oxygen transfer capacity within 8 s. Fig. 10 shows that the existence of SO_2 in the reducing gas would cause a change in both the reduction and oxidization behaviors, although an increase in the oxygen transfer capacity. The OCM shows decreased oxidization and reduction rates due to sulfur poisoning, especially reaction at low temperatures.

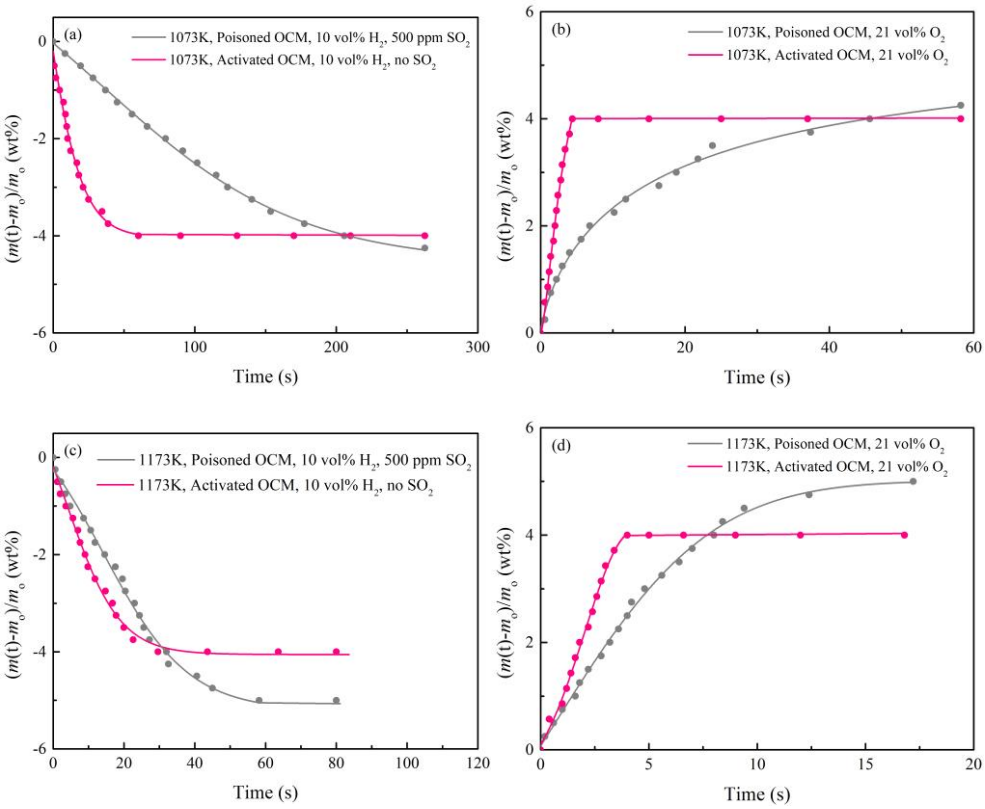

Fig. 10. Comparison of the reduction and oxidization reaction rates between the SO_2-poisoned and the activated OCM (the activated perovskite oxide is not treated by SO_2) at 1073 K and 1173 K. (a) reduction at 1073 K; (b) oxidization at 1073 K; (c) reduction at 1173 K; (d) oxidization at 1173K

From Figs. 11(a) and (b), the OCM can automatically recover from the SO_2-poisoning state once treating it with SO_2-absence fuel. Not only can the total transfer capacity be recovered to the original state, but also the recovered OCM shows the nearly same oxidization and reduction rates as the Activated OCM. Hence, it is quite interesting to notice that the investigated OCM possesses a chemical memory.

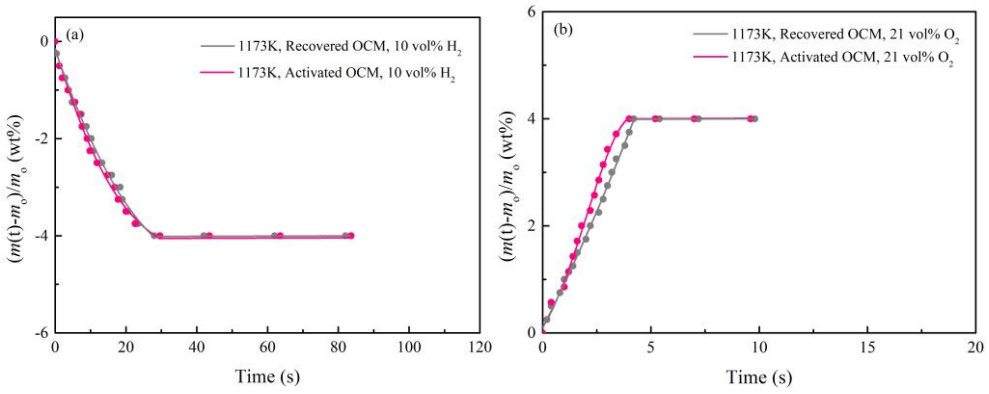

Fig. 11. Comparison of the (a) reduction and (b) oxidization reaction rates for the recovered and the activated OCM (the activated perovskite oxide is not treated by SO_2) at 1173 K.

4.3 Kinetic modelling results

The model results and experimental data of the oxidization reactions of the SO_2-poisoned and recovered OCMs are shown in Figs. 12(a) and (b). The conversion levels at different temperatures are plotted as a function of time. It is quite obvious that , the plots of conversion vs. time for the SO_2-poisoned OCM show two-stage behavior, i.e., an initially fast stage followed by a second slow stage. The model results agree well with experimental data. The reaction temperature has a significant effect on the critical conversion (ψX_e) and reaction rates for the oxidization step. Again, the calculated results could reproduce the experimental data obtained from the recovered OCM as well (Fig. 17(b)). Since the whole oxidization process merely has a fast stage, the value of ψ is set to 1 during the model calculation. The required time for the full oxidization is only ~4 s. The oxidization rate is insensitive to the temperature. The above kinetic behaviors of the oxidization reactions are similar to our previous work [26], where the reaction kinetics was driven by the activated OCM under the SO_2-free fuel, which implies that the oxidization performance is completely regenerated from the SO_2-poisoned state. After recovering from the SO_2-poisoning state, the chemical reaction rate constant (k_{chem}) for the oxidization reaction is higher than that of the

poisoned OCM, owing to the regeneration of the perovskite structure.

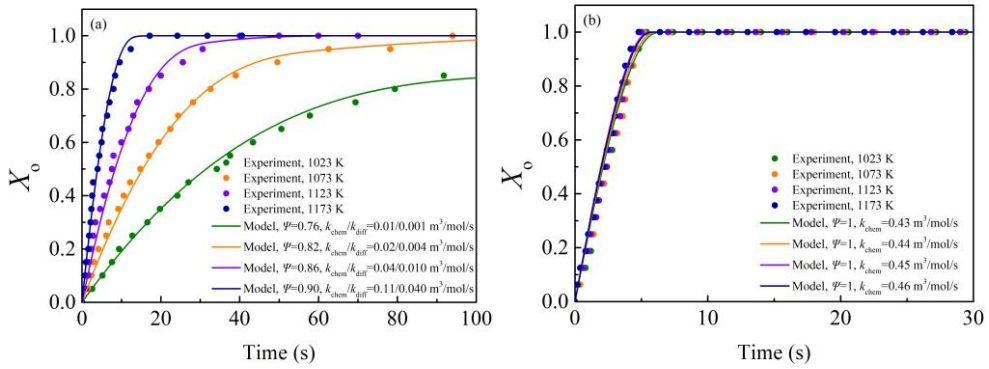

Fig. 12. Conversion versus time curves of the oxidization reactions of the (a) SO_2-poisoned and (b) recovered OCM at 1023-1173 K (oxidization: 21 vol% O_2)

Figs. 13(a) and (b) show the model and experimental results of the reduction reactions of the SO_2-poisoned and recovered OCM. The similarity between these two plots is that the reduction process consists of an initially fast stage followed by a second slow stage, like the oxidization of the SO_2-poisoned OCM. The distinction is that the reduction rate of the SO_2-poisoned OCM is apparently slower than that of the recovered OCM. For example, the full reduction needs ~160 s for the SO_2-poisoned OCM at 1123K, which is ~4 times slower than that of the recovered OCM. There is a significant effect of the reaction temperature on the critical conversions (ψX_e) for the reduction steps, and the reduction rate can be enhanced with increasing temperature. The kinetic behaviors of the reduction reactions are also similar to the activated OCM [26], because of the full release of the absorbed sulfur in the perovskite structure. As a result, the chemical reaction rate constants (k_{chem} and k_{diff}) for the reduction reaction are higher for the recovered OCM.

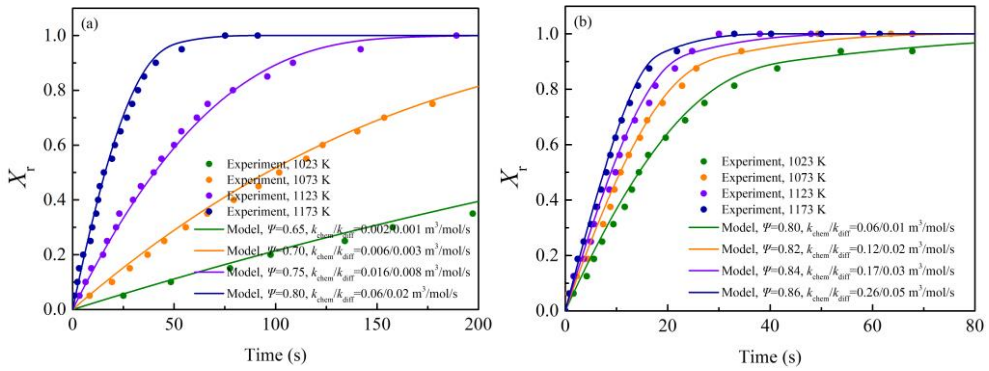

Fig. 13. Conversion versus time curves of the reduction reactions of the (a) SO_2-poisoned and (b) recovered OCM at 1023-1173 K (reduction: 10 vol% H_2)

From the Arrhenius plots of $\ln k_{chem}$, $\ln k_{diff}$, and $\ln \psi$ (Figs. 14(a)-(c)), the activation energies and pre-exponential factors can be obtained from the slopes and intercepts, respectively. The kinetic parameters are summarized in Table 4. Influenced by sulfur, the activation energies of the oxidization and reduction reactions of the SO_2-poisoned OCM are 156.64 kJ/mol and 222.56 kJ/mol at the first reaction stage, which is far higher than that of the recovered OCM, because of more sensitivity to the temperature. Table 4 also includes the kinetic parameters of the activated OCM obtained by similar reaction conditions [26]. Due to inherent chemical memory, the obtained kinetic parameters for the recovered OCM are similar as those of the activated OCM. According to the Arrhenius plots, the sulfur effect on the oxidization and reduction kinetics can be weakened with increasing temperature. For example, the sulfur effect on the reduction reactivity could be removed when elevating the temperature to ~1323 K. The above kinetic results are reliable since the oxygen transfer kinetics is faster than the oxygen consumption by the chemical reactions (Figs. S1-S4).

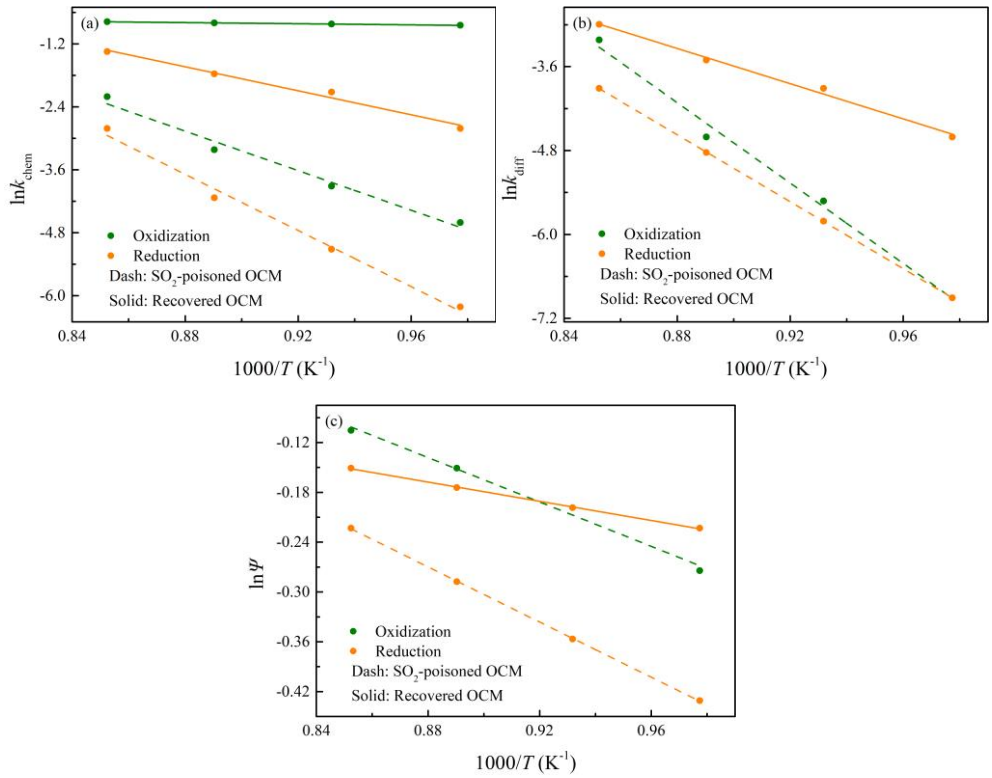

Fig. 14. Arrhenius plots of (a) $\ln k_{chem}$, (b) $\ln k_{diff}$, and (c) $\ln \psi$

Table 4. Summary of the kinetic parameters of the SO_2-poisoned, recovered, and activated OCM

	SO_2-poisoned OCM		Recovered OCM		Activated OCM[26]	
	O_2	H_2	O_2	H_2	O_2	H_2
A_{chem} (m^3/mol/s)	9.05×10^5	4.26×10^8	0.92	4.25×10^3	0.92	4.25×10^3
E_{chem} (kJ/mol)	156.64	222.56	6.69	94.17	6.69	94.17
A_{diff} (m^3/mol/s)	1.56×10^9	1.45×10^7	n.a.	1.62×10^3	n.a.	1.62×10^3
E_{diff} (kJ/mol)	238.89	199.04	n.a.	100.73	n.a.	100.73
A_ψ	2.82	3.26	n.a.	1.43	n.a.	1.43
E_ψ	11.12	13.81	n.a.	5.04	n.a.	5.04

4.4. Sample characterization

The fully oxidized and reduced particles extracted from variable redox cycle numbers in Fig.

5(b) were characterized by X-ray diffraction (XRD), see Figs. 15(a) and (b). The diffraction peaks of $CaSO_4$ (PDF 37-1496) and CaS (PDF 08-0464) emerge under the reduction condition with SO_2 but disappear under the reduction condition without SO_2. The common crystal phases of the oxidized and reduced OCM particles are $CaMnO_{2.56}$ (PDF 45-1267) and $CaFeTi_2O_6$ (PDF 83-0265), and the distinction is $CaMnO_3$ (PDF 03-0830) from the oxidized one and $CaTiO_3$ (PDF 082-0228) from the reduced one.

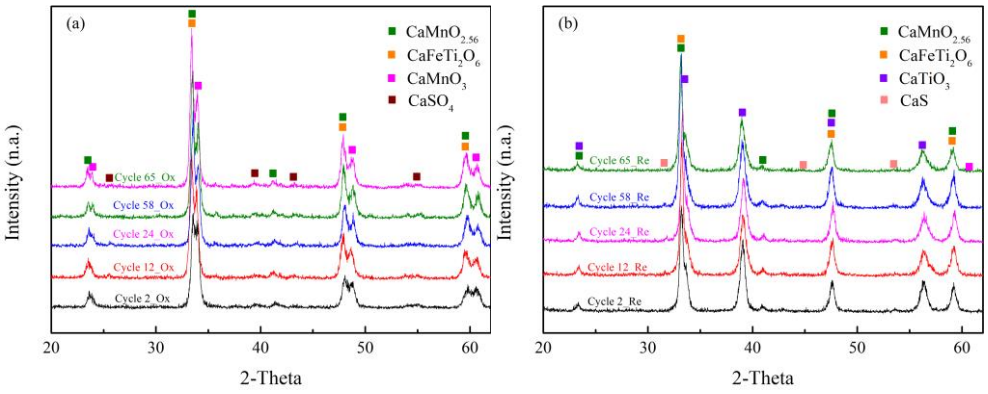

Fig. 15. X-ray diffraction patterns of the (a) oxidized and (b) reduced perovskite oxide at different cycles (cycle 2, 12, 24, 58, 65) in Fig. 5(b)

In situ diffuse reflectance infrared Fourier transform spectroscopy (in-situ DRIFTS) also shows that the $CaSO_4$ phase (1131.72 cm^{-1} and 1171.11 cm^{-1}) is gradually formed on the OCM particle surface under the reduction condition with SO_2, as shown in Fig. 16. Therefore, the gained mass in Fig.5(b) is also contributed by the sulfate and sulfide. The added oxygen transfer capacity due to formation of $CaSO_4$/CaS on the surface of oxygen carrier brings the oxygen transfer capacity to 5 wt% during the redox cycles under the reduction condition with SO_2. The profiles in Figs. 6(a) and 6(b) show sulfur effect leads to an increase in the oxygen transfer capacity from 4 wt% to 5 wt%, while the mass increased by ~ 6 wt% (Fig. 6(a)). If this is CaO to CaS and all CaS formed is ideally active, the one should expect the formation of $CaSO_4$ to give an increase in the oxygen transfer

capacity of 24 wt%. Actually, only 1 wt% oxygen transfer capacity was obtained due to sulfur effect. The possible explanation is the CaS to $CaSO_4$ oxidation has a low CaS conversion, and high percentage of the CaS reactant remains in the solid residues, according to Madarasz et al. [35] and Wang et al. [36].

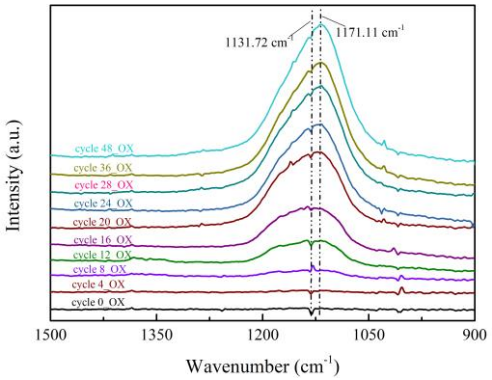

Fig. 16. In situ diffuse reflectance infrared Fourier transform spectroscopy (In situ-DRIFTS) during redox cycles

The scanning electron microscopy (SEM) images of the oxidized and reduced particles from various redox cycle numbers indicate that the particle surface is gradually covered by a white shell after reduction condition with exposure to SO_2, as depicted in Figs. 17(a) and (b). The grain boundary on the particle gradually becomes invisible due to the formation and coverage of the white shell. According to the energy dispersive spectrometer (EDS) results, the “white” sections on the particles are the enrichment region of oxygen (O), sulfur (S), and calcium (Ca) for the oxidized OCM and the enrichment region of sulfur (S) and calcium (Ca) for the reduced one, as seen in Figs. S5 and S6. Therefore, the components of the white shells on the oxidized and reduced OCM particle are identified as sulfate and sulfide respectively, which agrees well with the XRD patterns and in situ-DRIFTS results. Note that the formed shell is not very dense at sulfur -saturated state. After exposure to the reduction condition without SO_2, the sulfate and sulfide shells will gradually disappear, and the OCM particle can restore to the original state.

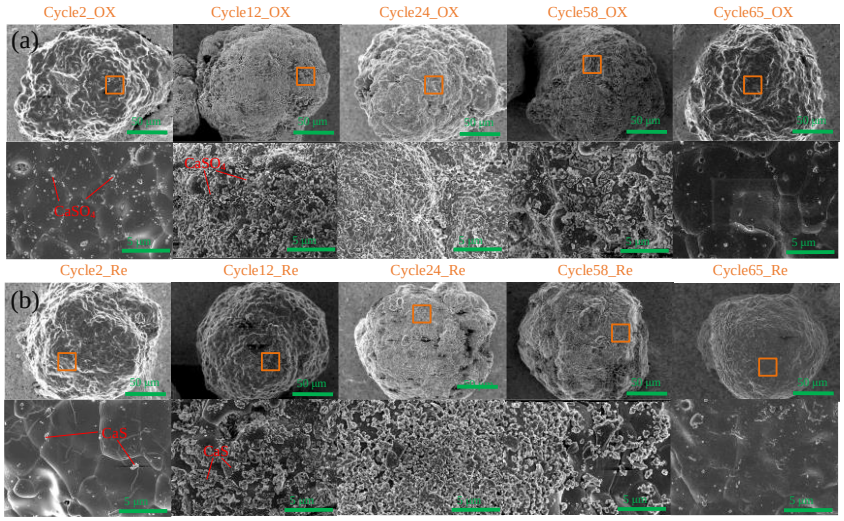

435

436 Fig. 17. Scanning electron microscopy images of the (a) oxidized and (b) reduced OCM

437 particles at different cycles (cycle 2, 12, 24, 58, 65) in Fig. 5(b)

438 To identify whether the bulk of the OCM particle is affected by the sulfur (S) element, energy

439 dispersive spectrometer (EDS) mapping of the particle cross-sections was further performed. With

440 the increasing redox cycle, sulfur (S) element was gradually accumulated on the particle surface as

441 a sulfate/sulfide shell, c.f. Figs. 18(a) and (b). Meanwhile, the average distribution of the sulfur (S)

442 elements was detected inside the OCM particle as well. The sulfur (S) element ratio of the surface

443 to the bulk is approximately 15:1 (Fig. S7), indicating that the sulfur (S) element is mainly enriched

444 on the particle surface. Such enrichment of sulfur (S) element on the shell shows that the OCM

445 particle possesses sulfur tolerance and self-protection ability. Nevertheless, a small amount of sulfur

446 (0.06 wt%) still affected the lattice structure inside the OCM particle, possibly caused by SO_2

447 molecules entering the particle inside through the pores or grain boundaries during the reduction

448 process.

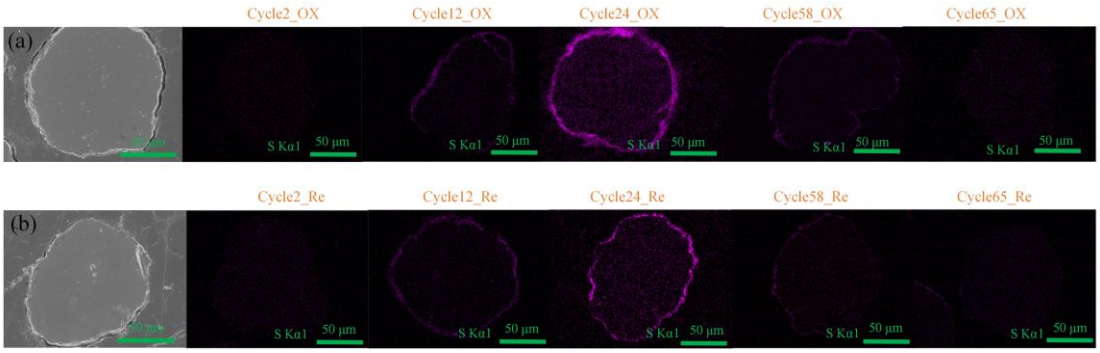

Fig. 18. Sulfur (S) element distribution in the cross-sections of the (a) oxidized and (b) reduced OCM particles at different cycles (cycle 2, 12, 24, 58, and 65) in Fig. 5

4.5 Possible Mechanism

To conclude, the whole OCM particle is initially the perovskite oxide. When the OCM particle is exposed to the reduction condition with SO_2, the particle surface would form a non-dense sulfate/sulfide shell, which wraps the OCM particle. The core is weakly affected by sulfur. Hence a shell-core structure forms under the reduction condition with SO_2. The reaction gas molecules can still contact the OCM particle through the non-dense shell. Once reduced in the reduction condition without SO_2, almost all sulfur in the shell and core will be gradually released from the particle. Finally, the shell-core structure disappears, and the whole OCM particle restores to its initial state, as illustrated in Fig. 19.

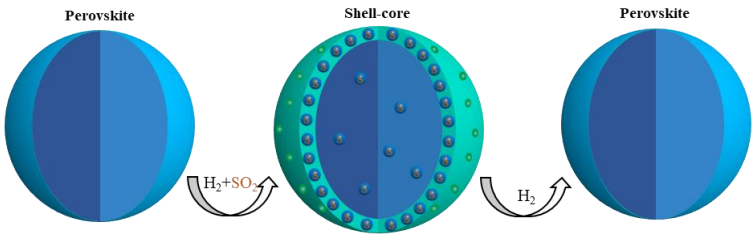

Fig. 19. The formation and disappearance of the non-dense sulfate/sulfide shell

The effect of sulfur on the chemical reactions can be diagramed in Fig. 20. On the reactant surface of the activated OCM, the oxygen anions can be smoothly exchanged with H_2 or O_2 through gas-solid reactions. Hence, both the reduction and oxidization rates are fast. Exposing to the

reduction condition with SO_2 brings chemical stress on the perovskite structure, as a result of the formation of sulfide via reaction R1. During the oxidization step, sulfide will be oxidized to sulfate via reaction R2. Sulfate and sulfide are thermodynamically more stable in the reduction condition [23]. As a result, the surface of the perovskite is affected by the absorbed sulfur, resulting in lower chemical performance, since the formed sulfate/sulfide formed will reduce the oxygen surface exchange. Hence, the OCM shows sulfur-poisoning effect. Comparatively, the absorbed sulfur is capable of being released in the form of H_2S after reaction with SO_2-uncontaining fuel via reaction R3, as a terrible smell was detected during the experiments. Another regeneration is possibly via reaction R4, accompanied by the formation of SO_2. Some SO_2 might get reduced through the combustion of H_2 and form H_2S and H_2O (R5), where the amount is related to eventual need for oxygen polishing. Finally, the perovskite structure can be fully recovered by subsequent redox cycles, and the chemical performance can be regenerated again.

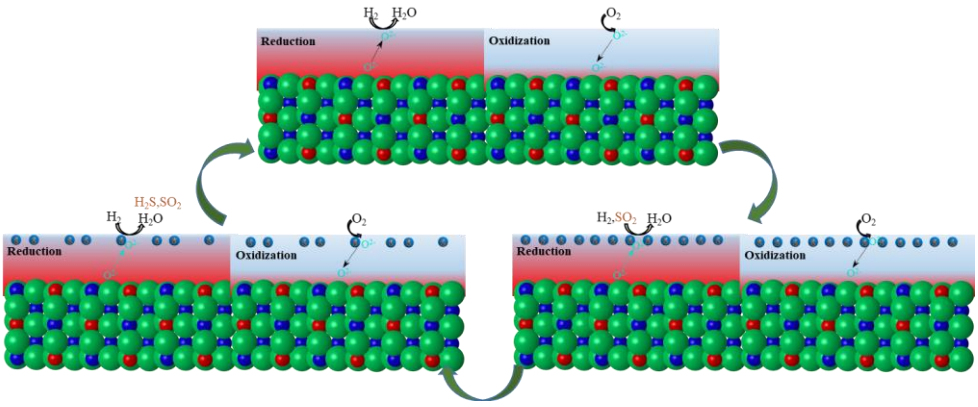

Fig.20. Schematic illustrations of the sulfur-poisoning and recovery process in the perovskite structure (red: calcium; blue: manganese/iron/titanium; green: oxygen)

$$CaO+3H_2+SO_2 \rightarrow CaS+3H_2O \quad \text{R1}$$

$$CaS+2O_2 \rightarrow CaSO_4 \quad \text{R2}$$

$$CaSO_4+4H_2 \rightarrow CaO+H_2S+3H_2O \quad \text{R3}$$

$$CaSO_4 + H_2 \rightarrow CaO + SO_2 + H_2O \quad \text{R4}$$

$$SO_2 + 3H_2 \rightarrow H_2S + 2H_2O \quad \text{R5}$$

5. Conclusions

The effect of sulfur in reduction species on oxygen transfer capacity and heterogeneous redox kinetics of a $CaMn_{0.375}Ti_{0.5}Fe_{0.125}O_{3-\delta}$ perovskite oxygen carrier was studied by using the micro-fluidized bed thermogravimetric analysis (MFB-TGA) technology. The results show that the sulfur can enhance the oxygen transfer capacity to 5 wt% from the original 4 wt %, but impede both the oxidization and reduction rates for the temperatures lower than 1173 K. When the temperature is higher than 1173 K, the sulfur has almost no effect on the H_2 reduction kinetics, but the oxidation kinetics decreases by 50% as compared to that of without sulfur. Nevertheless, the oxidation for the poisoned OCM is still fast enough and can achieve 4 wt% oxygen transfer capacity within 8 seconds. Once removing the SO_2 in the reducing gas, the oxygen transfer capacity and chemical performance are capable of being completely restored. The $CaMn_{0.375}Ti_{0.5}Fe_{0.125}O_{3-\delta}$ perovskite oxygen carrier possesses an interestingly chemical memorable ability under alternative reduction condition with and without SO_2. There is a significant effect of the reaction temperature on the critical conversions and reaction rates for the oxidization and reduction steps, except for the oxidization of the recovered OCM. The heterogeneous reaction kinetics at different temperatures was successfully modeled by the bubble bed reactor model coupled with a two-stage kinetic model, and the kinetic parameters, activation energies and pre-exponential factors were obtained from modelling. It was found that the reaction activation energies increase due to the effect of SO_2. And elevating temperature would remove SO2 poisoning effect. Combining X-ray diffraction (XRD), in situ diffuse reflectance infrared Fourier transform spectroscopy (in-situ DRIFTS), and scanning electron microscopy-

energy dispersive spectrometer (SEM-EDS), we revealed that the majority of sulfur (S) formed a sulfate/sulfide shell on the particle surface, whereas the minority sulfur (S) entered the particle interior and further affected the lattice structure. The perovskite structure was capable of totally automatic recovery from the poisoned state as well, by means of continuous redox cycles without SO_2.

ACKNOWLEDGMENTS

This work acknowledges the National Natural Science Foundation of China (51976102), the National Key Research and Development Plan of China (2016YFB0600802-A and 2017YFE0112500), and the European Union's Horizon 2020 Research and Innovation Program (764697- CHEERS).

Nomenclature

A_{chem}	pre-exponential factor of the fast reaction stage, $m^3/mol/s$
A_{diff}	pre-exponential factor of the slow reaction stage, $m^3/mol/s$
A_L	pre-exponential factor of the critical conversion
$C_{b,i}$	concentration of gas *i* in the bubble phase, mol/m^3
$C_{e,i}$	concentration of gas *i* in the emulsion phase, mol/m^3
$C_{eq,i}$	equilibrium concentration of gas *i*, mol/m^3
d_p	diameter of the oxygen carrier particle, m
D_i	gas *i* molecular diffusivity, m^2/s
E_{chem}	activation energy of the fast reaction stage, kJ/mol
E_{diff}	activation energy of the slow reaction stage, kJ/mol
E_L	activation energy of the critical conversion, kJ/mol

f_a	volume fraction of oxygen carrier particles in all solid volume
k_{chem}	reaction rate constant of the fast reaction stage, m^3/mol/s
k_{diff}	reaction rate constant of the slow reaction stage, m^3/mol/s
k_g	external mass transfer coefficient, m/s
K_{be}	interchange coefficient between the bubble and emulsion phase, s^{-1}
K_r	reaction rate constant of particles in the emulsion phase, s^{-1}
K_{ri}	reaction rate constant of particles, s^{-1}
$m(t)$	mass measured by the weight transducer at time t, g
m_o	whole mass of the reactor and oxidized oxygen carrier samples, g
m_{OC}	mass of the added oxygen carrier samples, g
m_r	whole mass of the reactor and reduced oxygen carrier, g
M_i	molar mass of i, kg/mol
R_g	ideal gases constant, J/mol/K
$R_{OC,t}$	total oxygen transfer capacity, wt.%
Sh	Sherwood number
T	temperature in Kelvin, K
U_0	superficial gas velocity, m/s
U_b	bubble rise velocity, m/s
U_b^*	effective gas velocity in the bubble phase, m/s
U_{mf}	minimum fluidization velocity, m/s
X	conversion level of oxidation or reduction reaction at time t
X_{chem}	conversion level of the fast reaction stage at time t

X_{diff}	conversion level of the slow reaction stage at time t
X_e	equilibrium conversion level of an oxygen carrier
X_o	conversion level of oxidation reaction at time t
X_r	conversion level of reduction reaction at time t
α	stoichiometric coefficient
ρ_s	particle density of oxygen carrier, kg/m^3
ε_{mf}	voidage of fluidized bed
θ	fraction of the bubble phase
ψ	ratio of the conversion level at the fast reaction stage to the conversion level

REFERENCES

[1] L. Zeng, Z. Cheng, J. A. Fan, L. S. Fan, J. Gong, Metal oxide redox chemistry for chemical looping processes, Nat. Rev. Chem. 2(11) (2018) 349-364.

[2] A. Lyngfelt, B. Leckner, T. Mattisson, A fluidized-bed combustion process with inherent CO_2 separation; application of chemical-looping combustion, Chem. Eng. Sci. 56(10) (2001) 3101-3113.

[3] J. Adanez, A. Abad, F. Garcia-Labiano, P. Gayan, F. Luis, Progress in chemical-looping combustion and reforming technologies, Prog. Energ. Combust. 38(2) (2012) 215-282.

[4] M. Tang, L. Xu, M. Fan, Progress in oxygen carrier development of methane-based chemical-looping reforming: A review, Appl. Energy 151 (2015) 143-156.

[5] L. Liu, Z. Li, L. Wang, Z. Zhao, Y. Li, N. Cai, MgO–Kaolin-supported manganese ores as oxygen carriers for chemical looping combustion, Indust. Eng. Chem. Res. 59(15) (2019)7238-7246.

[6] M. Arjmand, H. Leion, T. Mattisson, A. Lyngfelt, Investigation of different manganese ores as

530 oxygen carriers in chemical-looping combustion (CLC) for solid fuels, Appl. Energy 113 (2014)
531 1883-1894.
532 [7] M. Luo, S. Wang, L. Wang, M. Lv, Reduction kinetics of iron-based oxygen carriers using
533 methane for chemical-looping combustion. J. Power Sources 270 (2014) 434-440.
534 [8] C. R. Forero, P. Gayán, F. García-Labiano, L. F. De Diego, A. Abad, J. Adánez, Effect of gas
535 composition in chemical-looping combustion with copper-based oxygen carriers: fate of sulphur,
536 Int. J. Greenh. Gas Con. 4(5) (2010) 762-770.
537 [9] P. Gayán, F. Luis, F. García-Labiano, J. Adánez, A. Abad, C. Dueso, Effect of support on
538 reactivity and selectivity of Ni-based oxygen carriers for chemical-looping combustion, Fuel 87(12)
539 (2008) 2641-2650.
540 [10] R. Siriwardane, H. Tian, T. Simonyi, J. Poston, Synergetic effects of mixed copper–iron oxides
541 oxygen carriers in chemical looping combustion, Fuel 108(2013) 319-333.
542 [11] V. Frick, M. Rydén, H. Leion, Investigation of Cu–Fe and Mn–Ni oxides as oxygen carriers for
543 chemical-looping combustion, Fuel Process. Technol. 150 (2016) 30-40.
544 [12] P. N. Mohammad, H. Leion, M. Rydén, T. Mattisson, Combined Cu/Mn oxides as an oxygen
545 carrier in chemical looping with oxygen uncoupling (CLOU), Energy fuels 27(10) (2013) 6031-
546 6039.
547 [13] X. Zhu, K. Li, L. Neal, F. Li, Perovskites as geo-inspired oxygen storage materials for chemical
548 looping and three-way catalysis: a perspective, Acs Catal. 8(9) (2018) 8213-8236.
549 [14] K. R. Poeppelmeier, M. E. Leonowicz, J. C. Scanlon, J. M. Longo, W. B. Yelon, Structure
550 determination of $CaMnO_3$ and $CaMnO_{2.5}$ by X-ray and neutron methods. J. Solid State Chem. 45(1)
551 (1982) 71-79.

552 [15] R. Ruhl, J. Song, V. Thoréton, S. P. Singh, K. Wiik, Y. Larring, H. J. Bouwmeester, Structure,
553 electrical conductivity and oxygen transport properties of perovskite-type oxides $CaMn_{1-x-y}Ti_x$
554 $Fe_yO_{3-\delta}$, Phys. Chem. Chem. Phys. 21(39) (2019) 21824-21835.
555 [16] W. Xing, M. L. Fontaine, Z. Li, J. M. Polfus, Y. Larring, C. Denonville, R. Bredesen,
556 Asymmetric tubular $CaTi_{0.6}Fe_{0.15}Mn_{0.25}O_{3-\delta}$ membranes: Membrane architecture and long-term
557 stability, J. Membrane Sci. 548 (2018) 372-379.
558 [17] A. Abad, A. Cabello, P. Gayán, F. García-Labiano, L. F. de Diego, T. Mendiara, J. Adánez,
559 Kinetics of $CaMn_{0.775}Ti_{0.125}Mg_{0.1}O_{2.9-\delta}$ perovskite prepared at industrial scale and its implication on
560 the performance of chemical looping combustion of methane, Chem. Eng. J. (2020) 124863.
561 [18] L. Liu, Z. Li, Z. Li, Y. Larring, N. Cai, Heterogeneous reaction kinetics of a perovskite oxygen
562 carrier for chemical looping combustion coupled with oxygen uncoupling, Chem. Eng. J. 128054
563 (2020).
564 [19] A. Abad, F. García-Labiano, P. Gayán, L. F. de Diego, J. Adánez, Redox kinetics of $CaMg_{0.1}Ti_{0.125}Mn_{0.775}O_{2.9-\delta}$ for chemical looping combustion (CLC) and chemical looping with oxygen
565 uncoupling (CLOU), Chem. Eng. J. 269 (2015) 67-81.
566
567 [20] Y. Larring, M. Pishahang, J. Tolchard, A. M. Lind, M. F. Sunding, R. E. Stensrød, K. Albertsen,
568 Fabrication process parameters significantly affect the perovskite oxygen carriers materials (OCM)
569 performance in chemical looping with oxygen uncoupling (CLOU), J.Therm. Anal. Calorim. 140
570 (2019) 1-13.
571 [21] M. Arjmand, A. Hedayati, A.M. Azad, H. Leion, M. Rydén, T. Mattisson, $Ca_xLa_{1-x}Mn_{1-y}M_yO_{3-\delta}$ (M = Mg, Ti, Fe, or Cu) as Oxygen Carriers for Chemical-Looping with Oxygen Uncoupling
572
573 (CLOU), Energy Fuels 27 (2013) 4097-4107.

574 [22] L. F. de Diego, A. Abad, A. Cabello, P. Gayán, F. García-Labiano, J. Adánez, Reduction and
575 oxidation kinetics of a $CaMn_{0.9}Mg_{0.1}O_{3-\delta}$ oxygen carrier for chemical-looping combustion, Ind. Eng.
576 Chem. Res. 53(1) (2014)., 87-103.
577 [23] M. Pishahang, Y. Larring, M. Sunding, M. Jacobs, F. Snijkers, Performance of Perovskite-Type
578 Oxides as Oxygen-Carrier Materials for Chemical Looping Combustion in the Presence of H2S.
579 Energy Tech. 4(10) (2016) 1305-1316.
580 [24] R. F. Pachler, S. Penthor, K. Mayer, H. Hofbauer, Fate of sulfur in chemical looping combustion
581 of gaseous fuels using a Perovskite oxygen carrier, Fuel 241 (2019) 432-441.
582 [25] A. Cabello, A. Abad, P. Gayán, L. F. de Diego, F. García-Labiano, J. Adánez, Effect of operating
583 conditions and H_2S presence on the performance of $CaMg_{0.1}Mn_{0.9}O_{3-\delta}$ perovskite material in
584 chemical looping combustion (CLC), Energy fuels 28(2) (2014) 1262-1274.
585 [26] L. Liu, Z. Li, Z. Li, Y. Larring, Y. Li, N. Cai, Fast redox kinetics of a perovskite oxygen carrier
586 measured using micro-fluidized bed thermogravimetric analysis, Proc. Combust. Inst. (2020).
587 [27] Y. Li, H. Wang, W. Li, Z. Li, N. Cai, CO_2 Gasification of a Lignite Char in Microfluidized Bed
588 Thermogravimetric Analysis for Chemical Looping Combustion and Chemical Looping with
589 Oxygen Uncoupling, Energy fuels 33(1) (2018) 449-459.
590 [28] Y. Li, Z. Li, L. Liu, N. Cai, Measuring the fast oxidation kinetics of a manganese oxygen carrier
591 using microfluidized bed thermogravimetric analysis, Chem. Eng. J. 385 (2020) 123970.
592 [29] D. Kunii, O. Levenspiel, Fluidization Engineering, Butterworth-Heinemann, Newton, U.S.A.
593 1991, p. 155.
594 [30] Z. Li, General rate equation theory for gas-solid reaction kinetics and its application to CaO
595 carbonation, Chem. Eng. Sci. 227(2020) 115902.

596 [31] D. K. Lee, An apparent kinetic model for the carbonation of calcium oxide by carbon dioxide,
597 Chem. Eng. J. 100(1-3) (2004) 71-77.
598 [32] M. Ishida, C. Y. Wen, Comparison of zone-reaction model and unreacted-core shrinking model
599 in solid—gas reactions—I isothermal analysis, Chem. Eng. Sci. 26(7) (1971) 1031-1041.
600 [33] S. K. Bhatia, D. D. Perlmutter, A random pore model for fluid-solid reactions: I. Isothermal,
601 kinetic control, AIChE J. 26(3) (1980) 379-386.
602 [34] J. C. Shelley, M. Y. Shelley, R. C. Reeder, S. Bandyopadhyay, M. L. Klein, A coarse grain
603 model for phospholipid simulations, J. Phys. Chem. B 105(19) (2001) 4464-4470.
604 [35] J. Madarász, T. Leskelä, J. Rautanen, L. Niinistö, Oxidation of alkaline-earth-metal sulfide
605 powders and thin films, J. Mater. Chem. 6(5) (1996) 781-787.
606 [36] M. Zheng, S. Zhong, K. Li, H. Wang, H. Liu, Y. Wei, X. Zhu, Characteristics of CaS-CaO
607 Oxidation for Chemical Looping Combustion with a $CaSO_4$-Based Oxygen Carrier, Energy Fuels
608 31(12) (2017) 13842-13851.